



Cite this: *Phys. Chem. Chem. Phys.*,  
2016, **18**, 19773

# The formation mechanism of eutectic microstructures in NiAl–Cr composites

Bin Tang,<sup>ab</sup> Daniel A. Cogswell,<sup>†c</sup> Guanglong Xu,<sup>b</sup> Srdjan Milenkovic<sup>b</sup> and Yuwen Cui<sup>\*bd</sup>

NiAl-based eutectic alloys, consisting of an ordered bcc matrix (B2) and disordered bcc fibers (A2), have been a subject of intensive efforts aimed at tailoring the properties of many of the currently used nickel-based superalloys. A thermodynamic phase field model was developed on a thermodynamic foundation and fully integrated with a thermo-kinetic database of the Ni–Al–Cr ternary system to elucidate the resulting peculiar eutectic microstructure. Invoking a variation of the liquid/solid interfacial thickness with temperature, we simulated the characteristic sunflower-like eutectic microstructures in the NiAl–Cr composites, consistent with experimental observations. The mechanism that governs the formation of the peculiar eutectic morphology was envisioned from the modeled evolutions associated with six sequential steps. Our calculations show that the conditional spinodal decomposition occurring in sequence could further trim and revise the microstructure of the eutectics by generating fine-domain structures, thereby providing an additional method to explore the novel NiAl-based eutectic composites with tunable properties at elevated temperatures.

Received 22nd March 2016,  
Accepted 17th June 2016

DOI: 10.1039/c6cp01921h

www.rsc.org/pccp

## 1. Introduction

NiAl-based composites are considered to be among the most important candidates to replace the current state-of-the-art Ni-based superalloys for structural applications in turbine engines due to their low density, high melting temperature, good thermal conductivity and excellent oxidation resistance at elevated temperatures.<sup>1,2</sup> However, the application of NiAl based alloys is limited due to the natural weakness of intermetallic compounds, *e.g.* poor ductility and fracture resistance at ambient temperatures and inferior strength and creep resistance at elevated temperatures.<sup>3,4</sup> In order to obtain desirable comprehensive properties, ternary and quaternary NiAl-based eutectic composites were recently developed and fabricated by directional solidification.<sup>5–8</sup> For the NiAl–RM (RM is a refractory metal such as Cr, Mo, V, W, Nb or Re) based eutectic composites, the A2 (*i.e.* b.c.c. for  $\alpha$ -RM) lamellae rich in refractory metals align themselves as reinforcements in the B2–NiAl (*i.e.* CsCl for  $\beta$ -NiAl) matrix, contributing to improved toughness and creep strength.

The NiAl–Cr composite, the base alloy of the NiAl eutectic family,<sup>9,10</sup> has been investigated to optimize its mechanical properties, but the formation mechanism of the distinctive solidified eutectic microstructure remains uncertain largely due to the inherent complexity of eutectic solidification for the multicomponent multi-phase system. The phase field approach, when linked to thermodynamic and/or kinetic databases in the framework of the CALPHAD method, has proven effective in understanding the formation mechanism of microstructures such as those resulting from precipitation<sup>11</sup> and solidification.<sup>12–14</sup> Differing from the popular multi-phase field model,<sup>13–22</sup> we extend the thermodynamic phase field model developed by Cogswell and Carter,<sup>23</sup> which is capable of simulating phenomena that depend on the width of the diffuse interface. Besides, the conditional spinodal decomposition occurring after eutectic solidification was analyzed based on thermodynamic calculations.<sup>24,25</sup> It is in this work that we deal with the NiAl–Cr ternary alloys to understand the microstructure developed by eutectic solidification. This is also in view of the abundant experimental observations, for example ref. 5 and 26, and feasible thermo-kinetic (both thermodynamic<sup>27</sup> and mobility<sup>28</sup>) databases, which could enable a quantitative description of the thermodynamic phase field model and immediate validation against experimental observations.

## 2. A2 + B2 eutectic microstructure in NiAl–Cr composites

The eutectic microstructure of NiAl based composites, typically consisting of RM-rich A2 fine fibers embedded in a B2–NiAl

<sup>a</sup> State Key Laboratory of Solidification Processing, Northwestern Polytechnical University, Xi'an 710072, P. R. China

<sup>b</sup> IMDEA Materials Institute, c/Eric Kandel, 2, Getafe 28906, Madrid, Spain

<sup>c</sup> Department of Materials Science & Engineering, Massachusetts Institute of Technology, Cambridge, MA 02139, USA

<sup>d</sup> Institute for Advanced Metallic Materials & School of Materials Science and Engineering, Nanjing Tech University, Nanjing 210009, China.  
E-mail: ycu@njtech.edu.cn

<sup>†</sup> Present address: Aramco Research Center-Boston, 400 Technology Square, Cambridge, Massachusetts 02139, USA.

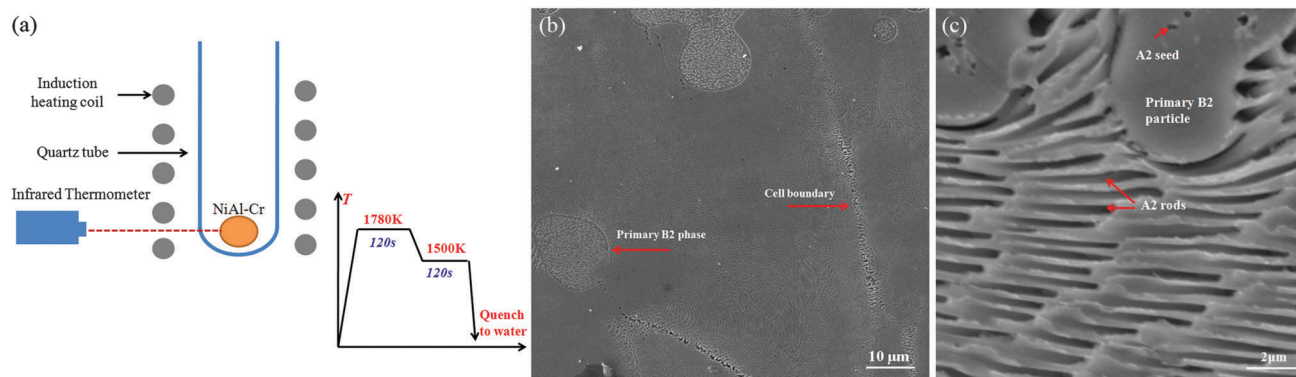


Fig. 1 (a) The isothermal solidification process to fabricate the NiAl–Cr alloy in this work; (b) the secondary electron image of the etched Ni–33.5%Al–33%Cr (at%) alloy obtained by isothermal solidification at 1500 K; (c) the enlarged view of a typical microstructure consisting of A2 rods, primary B2 phases and A2 seeds.

matrix, has been critically reviewed by Noebe and Walston.<sup>26</sup> It is believed that near-equilibrium microstructure and very fine eutectic spacing result in eutectic composites with superb melting temperatures and excellent high-temperature creep resistance. Detailed investigation<sup>5</sup> revealed that the eutectic rods grow roughly perpendicular to the  $\langle 100 \rangle$  oriented B2 grains, through spinodal decomposition, further changing into a fine microstructure with an average wavelength of 10 nm that deviates slightly with the addition of RM (Mo, V and W).<sup>29</sup> A recent observation of the near-eutectic  $\text{Ni}_2\text{Al}_2\text{CrCuFe}$  alloy termed the appearance of the eutectic colony as “sunflower-like” microstructure,<sup>30</sup> with the primary B2 phase as the disk floret (*i.e.* fiber in a wider sense), the decomposed A2 rods as petals, and the A2 particles as seeds. The microstructure containing numerous “sunflowers” has been obtained by Sheng *et al.* in the NiAl–Cr(Mo) near eutectic alloy prepared by suction casting.<sup>31</sup>

It was clearly established<sup>24</sup> that the phase separation in Fe-rich iron aluminides could occur contingently on prior B2 ordering transition, termed as “conditional spinodal decomposition” (CSD), leading to the formation of a mixture of B2 and disordered A2. Likewise, because of the presence of a A2/B2 second-order transition in the NiAl–Cr pseudo-binary phase diagram, as its prototype FeAl alloys, there should be an A2/B2 second-order transition line intersecting with a spinodal of the B2 order phase, thus inherently giving rise to a tricritical point. Because the morphology of NiAl–Cr composites near the tricritical point, roughly estimated at (40 at% Cr, 2400 K), varies with the alloy compositions and quenching temperatures, a number of possible phase transformation mechanisms may be possible.

To this end, a NiAl–Cr (33.5%Ni–33.5%Al–33.0%Cr (at%)) ingot alloy 30 g in weight was prepared from 99.99% Ni, 99.99% Al and 99.99% Cr (mass%) by arc melting under vacuum. A cylindrical sample, *i.e.* 1/3 of the length of the same diameter as the original ingot, was cut and placed in a quartz tube for an isothermal solidification process depicted in Fig. 1(a) in an induction furnace. The sample was then prepared for microstructural characterization by conventional metallographic techniques and imaged by scanning electron microscopy (SEM: Helios Nano Lab 600i, FEI). The solidified microstructure of NiAl–Cr is

typified in Fig. 1(b and c). It consists of the primary B2 disk, the ultra fine rod-like (A2 + B2) eutectic and A2 seeds within the primary B2 disk. The development of this microstructure is thought to be in three sequential events: the formation of supersaturated B2 by partitionless solidification, the fine rod eutectic solidification of (A2 + B2) and the intergranular A2 at the liquid–solid interface based on the disordered (b.c.c.) nature of the APBs themselves.

### 3. Thermodynamic phase field model

#### 3.1 Governing equations

Three phases (A2, B2 and liquid) and three components (Al, Cr and Ni) are considered in the present model. The spatio-temporal evolution of the three phases follows Allen–Cahn dynamics:<sup>32</sup>

$$\frac{\partial \varphi_\alpha}{\partial t} = -M_\varphi \cdot \frac{\delta \bar{F}}{\delta \varphi_\alpha} \quad (1)$$

in which  $\varphi$  is the order parameter,  $M_\varphi$  is the interface mobility and  $\bar{F}$  is the molar quantity of free energy ( $F$ ). By considering isotropic and cubic symmetry of free energy and ignoring the energy penalty for overlapping phase and concentration gradients, Cagwell developed a multiphase, multicomponent free energy function.<sup>23</sup>

$$F[\{x\}, \{\varphi\}] = \int_V \left[ f_0 + \sum_{\alpha, \beta=1}^{N-1} \frac{1}{2} \lambda_{\alpha\beta} \vec{\nabla} \varphi_\alpha \cdot \vec{\nabla} \varphi_\beta + \sum_{i,j=1}^{M-1} \frac{1}{2} k_{ij} \vec{\nabla} x_i \cdot \vec{\nabla} x_j \right] dV \quad (2)$$

where the homogeneous free energy density  $f_0$  is

$$f_0 = \sum_{\alpha=1}^N \varphi_\alpha G^\alpha(\{c\}, T) + \sum_{\beta \neq \alpha} W_{\alpha\beta} \varphi_\alpha \varphi_\beta, \quad (3)$$

and  $\lambda_{\alpha\beta}$  and  $k_{ij}$  are the coefficients of the phase field and solute gradient energies, respectively.  $M$  and  $N$  are the total number of components and phases in the alloys, respectively.  $G^\alpha(x, T)$  is the free energy density of the  $\alpha$  phase with composition  $\{x\}$  and temperature  $T$ . We assume that at every point in space we have

the coexistence of a three-phase mixture ( $\alpha$  = liquid, A2 and B2) under the linear weighting rule with respect to the phase fraction.  $W_{\alpha\beta}$  is the height of the double well potential. Therefore, the phase evolution equations can transform to

$$\frac{\partial \varphi_\alpha}{\partial t} = -M_\varphi \cdot \left( \frac{\partial f_0}{\partial \varphi_\alpha} - \sum_{\beta=1}^{N-1} \lambda_{\alpha\beta} \nabla^2 \varphi_\beta \right) \quad (4)$$

In the present model, the interfacial thickness is assumed not to depend on crystal orientation. Thus, the system is effective in order to treat interfacial isotropic problems. The component evolution equations for the ternary system are described by Cahn–Hilliard equations. According to Campbell's study with respect to diffusion mobilities in the Ni–Al–Cr system,<sup>28</sup> the effect of cross diffusion cannot be ignored. The interdiffusion flux of component ( $i$ ) generalized from Fick's first law and the Gibbs–Duhem relation can be written as follows:<sup>33</sup>

$$\vec{J}_i = -\tilde{M}_{ii} \nabla \hat{\mu}_i - \tilde{M}_{ij} \nabla \hat{\mu}_j \quad (5)$$

where  $\hat{\mu}$  is the inhomogeneous chemical potential,  $\tilde{M}_{ii}$  and  $\tilde{M}_{ij}$  are the chemical mobilities of the ternary system, defined as the function of the atomic mobility  $M_i$ ,<sup>34,35</sup>

$$\tilde{M}_{ii} = V_m^{-1} \{ (1 - x_i) x_i M_i - x_i [(1 - x_i) x_i (M_i - M_{Ni}) - x_i x_j (M_j - M_{Ni})] \} \quad (6)$$

$$\tilde{M}_{ij} = V_m^{-1} \{ -x_i x_j M_j - x_j [(1 - x_i) x_i (M_i - M_{Ni}) - x_i x_j (M_j - M_{Ni})] \} \quad (7)$$

By considering the mole fraction constraint  $x_{Al} + x_{Cr} + x_{Ni} = 1$ , the variational derivatives of free energy with respect to  $x_i$  become<sup>23</sup>

$$\left( \frac{\delta \bar{F}}{\delta x_{Al}} \right)_{T,V,x_{Cr}} = \hat{\mu}_{Al} - \hat{\mu}_{Ni} \quad (8)$$

$$\left( \frac{\delta \bar{F}}{\delta x_{Cr}} \right)_{T,V,x_{Al}} = \hat{\mu}_{Cr} - \hat{\mu}_{Ni} \quad (9)$$

where  $x_{Al}$ ,  $x_{Cr}$  and  $x_{Ni}$  are the contents of Al, Cr and Ni, respectively. By considering the Gibbs–Duhem relation and eliminating  $x_{Ni}$ , the  $\vec{\nabla} \hat{\mu}_i$  can be obtained as:

$$\vec{\nabla} \hat{\mu}_{Al} = (1 - x_{Al}) \vec{\nabla} \frac{\delta \bar{F}}{\delta x_{Al}} - x_{Cr} \vec{\nabla} \frac{\delta \bar{F}}{\delta x_{Cr}} \quad (10)$$

$$\vec{\nabla} \hat{\mu}_{Cr} = (1 - x_{Cr}) \vec{\nabla} \frac{\delta \bar{F}}{\delta x_{Cr}} - x_{Al} \vec{\nabla} \frac{\delta \bar{F}}{\delta x_{Al}} \quad (11)$$

Therefore, the flux of components Al and Cr can be written as:

$$\begin{aligned} \vec{J}_{Al} = & -\tilde{M}_{AlAl} \left( (1 - x_{Al}) \vec{\nabla} \frac{\delta \bar{F}}{\delta x_{Al}} - x_{Cr} \vec{\nabla} \frac{\delta \bar{F}}{\delta x_{Cr}} \right) \\ & - \tilde{M}_{AlCr} \left( (1 - x_{Cr}) \vec{\nabla} \frac{\delta \bar{F}}{\delta x_{Cr}} - x_{Al} \vec{\nabla} \frac{\delta \bar{F}}{\delta x_{Al}} \right) \end{aligned} \quad (12)$$

$$\begin{aligned} \vec{J}_{Cr} = & -\tilde{M}_{CrAl} \left( (1 - x_{Al}) \vec{\nabla} \frac{\delta \bar{F}}{\delta x_{Al}} - x_{Cr} \vec{\nabla} \frac{\delta \bar{F}}{\delta x_{Cr}} \right) \\ & - \tilde{M}_{CrCr} \left( (1 - x_{Cr}) \vec{\nabla} \frac{\delta \bar{F}}{\delta x_{Cr}} - x_{Al} \vec{\nabla} \frac{\delta \bar{F}}{\delta x_{Al}} \right) \end{aligned} \quad (13)$$

in which  $\tilde{M}_{AlCr} = \tilde{M}_{CrAl}$ .

The diffusion equations for the NiAl–Cr ternary system can be expressed by the continuity equation:

$$\frac{\partial x_i}{\partial t} = -\vec{\nabla} \cdot \vec{J}_i \quad (i = Al, Cr) \quad (14)$$

Substitution of eqn (12) and (13) produces the component evolution equations for NiAl–Cr composites:

$$\begin{aligned} \frac{\partial x_{Al}}{\partial t} = & \vec{\nabla} \cdot \left\{ [\tilde{M}_{AlAl}(1 - x_{Al}) - \tilde{M}_{AlCr} \cdot x_{Al}] \cdot \vec{\nabla} \frac{\delta \bar{F}}{\delta x_{Al}} \right. \\ & \left. - [\tilde{M}_{AlAl} \cdot x_{Cr} - \tilde{M}_{AlCr}(1 - x_{Cr})] \cdot \vec{\nabla} \frac{\delta \bar{F}}{\delta x_{Cr}} \right\} \end{aligned} \quad (15)$$

$$\begin{aligned} \frac{\partial x_{Cr}}{\partial t} = & \vec{\nabla} \cdot \left\{ [\tilde{M}_{CrAl}(1 - x_{Al}) - \tilde{M}_{CrCr} \cdot x_{Al}] \cdot \vec{\nabla} \frac{\delta \bar{F}}{\delta x_{Al}} \right. \\ & \left. - [\tilde{M}_{CrAl} \cdot x_{Cr} - \tilde{M}_{CrCr}(1 - x_{Cr})] \cdot \vec{\nabla} \frac{\delta \bar{F}}{\delta x_{Cr}} \right\} \end{aligned} \quad (16)$$

where the variational derivative  $\delta \bar{F} / \delta x_i$  can be found by applying the Euler–Lagrange equation to the multiphase multicomponent free energy function.

$$\frac{\delta \bar{F}}{\delta x_i} = \sum_{\alpha=1}^3 \varphi_\alpha \frac{\partial G^\alpha}{\partial x_i} - \sum_{j=1}^2 k_{ij} \nabla^2 x_j \quad (i, j = Al, Cr) \quad (17)$$

The phase field model developed in a thermodynamically consistent way consists of eqn (4), (15) and (16). This model correctly captures solute trapping and spinodal decomposition because a compositional gradient energy is included.

Three distinct phase transformations are considered in our eutectic solidified model: transformation from liquid into the two solids (A2 and B2), and transformation between A2 and B2. Due to the free energy of A2 and B2 modeled in a single equation as a function of composition, the transformations between A2 and B2 are represented by nonlinear diffusion equations. In order to quantitatively describe the order–disorder transformation between the A2/B2 phases, a single CALPHAD-based Gibbs energy function upon the modified sublattice formalism was incorporated into our model, which is a sum of the Gibbs energy of the disorder A2 and an ordering contribution of the ordered B2 phases.<sup>27</sup> As in the spirit of the CALPHAD method, the atomic mobility of the B2 phase was also modeled with a single formalism for A2 by adding the activation energy of diffusion with an excess chemical ordering contribution.<sup>28</sup>

### 3.2 Linking the chemical free energy from the thermodynamic database to the phase field model

On the basis of the CALPHAD technique, the molar Gibbs free energy of liquid and A2 phases is derived from a ternary regular solution model having the following general expression:<sup>36</sup>

$$G^{\alpha} = G_m^{\text{ref}} + \Delta_{\text{mix}} G_m^{\text{id}} + G^{\epsilon} \quad \alpha = \text{L, A2} \quad (18)$$

where  $G_m^{\text{ref}}$  is a reference free energy,  $\Delta_{\text{mix}} G_m^{\text{id}}$  is the ideal mixing contribution, and  $G^{\epsilon}$  is the excess Gibbs energy, which is expressed by a Redlich–Kister polynomial.<sup>37</sup> For the NiAl–Cr alloys, the three Gibbs energy terms of liquid and A2 phases are expressed as:

$$G_m^{\text{ref}} = x_{\text{Al}} {}^0G_{\text{m,Al}}^{\circ} + x_{\text{Cr}} {}^0G_{\text{m,Cr}}^{\circ} + x_{\text{Ni}} {}^0G_{\text{m,Ni}}^{\circ} \quad (19)$$

$$\Delta_{\text{mix}} G_m^{\text{id}} = RT(x_{\text{Al}} \ln x_{\text{Al}} + x_{\text{Cr}} \ln x_{\text{Cr}} + x_{\text{Ni}} \ln x_{\text{Ni}}) \quad (20)$$

$$G^{\epsilon} = x_{\text{Al}} x_{\text{Cr}} L_{\text{Al,Cr}}^{\circ} + x_{\text{Al}} x_{\text{Ni}} L_{\text{Al,Ni}}^{\circ} + x_{\text{Cr}} x_{\text{Ni}} L_{\text{Cr,Ni}}^{\circ} + x_{\text{Al}} x_{\text{Cr}} x_{\text{Ni}} L_{\text{Al,Cr,Ni}}^{\circ} \quad (21)$$

where  ${}^0G_{\text{m,Al}}^{\circ}$ ,  ${}^0G_{\text{m,Cr}}^{\circ}$  and  ${}^0G_{\text{m,Ni}}^{\circ}$  are the Gibbs free energies of the pure elements Al, Cr and Ni, respectively, at 298.15 K in their standard element reference (SER) state.  $L_{\text{Al,Cr}}^{\circ}$ ,  $L_{\text{Al,Ni}}^{\circ}$  and  $L_{\text{Cr,Ni}}^{\circ}$  are the binary interaction parameters between elements Al and Cr, Al and Ni, and Cr and Ni, respectively.  $L_{\text{Al,Cr,Ni}}^{\circ}$  is the ternary interaction parameter among Al, Cr and Ni.

For the ternary order phase, B2, it has been firstly modelled by a two sublattice (SL) formalism independent of the A2 solid solution.<sup>38</sup> Subsequently, in order to simplify the treatment of order–disorder transformation, Dupin developed a modified sublattice (MSL) formalism by combining SL with the Redlich–Kister (RK) equation.<sup>27,39</sup> It has the following form

$$G^{\text{A2 or B2}}(x_i y_i^{(s)}) = G^{\text{A2}}(x_i) + \Delta G^{\bullet \text{B2}}(y_i^{(s)}) - \Delta G^{\bullet \text{B2}}(y_i^{(s)} = x_i) \quad (22)$$

$$\Delta G^{\bullet \text{B2}}(y_i^{(s)}) = \sum_i \sum_j y_i' y_j'' G_{ij}^{\bullet \text{B2}} + \frac{1}{2} RT \left( \sum_i y_i' \ln y_i' + \sum_j y_j'' \ln y_j'' \right) \quad (23)$$

where  $y_i'$  and  $y_i''$  are the site fractions, representing mole fractions of species  $i$  and  $j$  on the two SL. For simplicity, we substitute  $x_1$ ,  $x_2$  and  $x_3$  for  $x_{\text{Al}}$ ,  $x_{\text{Cr}}$  and  $x_{\text{Ni}}$ , respectively. The sum of all elements on each SL must be equal to 1,  $\sum_{i=1}^3 y_i' = 1$  and  $\sum_{i=1}^3 y_i'' = 1$ , and  $G_{ij}^{\bullet \text{B2}}$  are binary ordering parameters. Thus

although there are six site fractions, only four of them are independent. In eqn (23), the A2 and B2 phases are modeled with a single equation. When the site fraction  $y_i^{(s)}$  is equal to the mole fraction  $x_i$ ,  $\Delta G^{\bullet \text{B2}}(y_i^{(s)})$  becomes identical to  $\Delta G^{\bullet \text{B2}}(y_i^{(s)} = x_i)$ , and the Gibbs energy  $G^{\text{A2 or B2}}$  represents the disordered A2 phase. Otherwise, it represents the ordered B2 phase as a function of site fractions and mole fractions.

As indicated by eqn (3), the local chemical free energy ( $f_0$ ) in the phase field model is a function of  $x_i$  and  $\phi_z$ . For the B2 phase, the six site fractions ( $y_1'$ ,  $y_2'$ ,  $y_3'$ ,  $y_1''$ ,  $y_2''$ , and  $y_3''$ ) can be determined through an internal equilibrium rule at a certain composition and temperature.

$$\frac{\partial \Delta G^{\bullet \text{B2}}}{\partial y_i^{(s)}} = 0 \quad (24)$$

In order to reduce the variables and simplify the expressions, we introduce four variables, departure degrees ( $\theta_1$  and  $\theta_2$ ) and long-range order degrees ( $\sigma_1$  and  $\sigma_2$ ), as substitutes for the six site fractions and three mole fractions.

$$\theta_1 = 2x_1 - 1 \quad (25a)$$

$$\theta_2 = 2x_3 - 1 \quad (25b)$$

$$\sigma_1 = y_1' - y_1'' \quad (25c)$$

$$\sigma_2 = y_3' - y_3'' \quad (25d)$$

If  $\theta_1 = \theta_2$ , then  $x_{\text{Al}} = x_{\text{Cr}}$ . If  $\sigma_1 = \sigma_2 = 0$ , then  $y_i' = y_j' = x_i$ . For an alloy where  $\theta_1$  and  $\theta_2$  are constants, eqn (25) can be reduced to

$$\frac{\partial \Delta G^{\bullet \text{B2}}}{\partial \sigma_1} = 0 \quad (26a)$$

$$\frac{\partial \Delta G^{\bullet \text{B2}}}{\partial \sigma_2} = 0 \quad (26b)$$

Then, the molar Gibbs free energy of the liquid, A2, and B2 phases described by eqn (18) and (23) can be quantitatively calculated by linking to the thermodynamic database of NiAl–Cr alloys (see Appendix A). The equilibrium free energy of the three phases at 1500 K and 1723 K is plotted in Fig. 2.

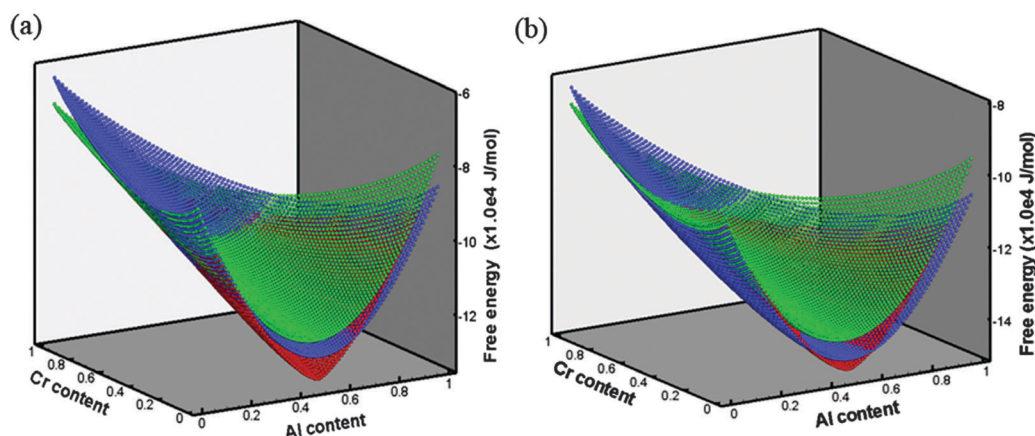


Fig. 2 The chemical free energy as a function of concentrations at 1500 K (a) and 1723 K (b) calculated by using eqn (18) and (23) from the thermodynamic database in Appendix A.



According to eqn (23) and (24), the partial derivatives of the local chemical free energy for the B2 phase with respect to the composition can be derived as follows:

$$\frac{\partial G^{\text{B2}}}{\partial x_i} = \frac{\partial G^{\text{A2}}}{\partial x_i} + \sum_{s=1}^2 \sum_{n=1}^3 \frac{\partial G^{\text{B2}}}{\partial y_n^{(s)}} \cdot \frac{\partial y_n^{(s)}}{\partial x_i} - \frac{\partial \Delta G^{\text{B2}}(y_i^{(s)} = x_i)}{\partial x_i} \quad i = 1, 2 \quad (27)$$

where  $y_n^{(s)}$  can be written as a function of  $(\theta_1, \theta_2, \sigma_1, \sigma_2)$ . Detailed derivation can be seen in Appendix B.

### 3.3 Linking the diffusion mobility from the kinetics database to diffusion equations

In the component evolution model (eqn (15) and (16)), the flux of each element is calculated using the chemical mobility matrix  $M_{ij}$ . For the NiAl–Cr ternary system, the mole fraction of Ni is chosen as dependent on the other elements. Therefore, the chemical mobility can be written as a function of atomic mobility,  $M_i$  ( $i = \text{Al, Cr and Ni}$ ), as expressed by eqn (6) and (7). In order to couple the diffusion mobility to diffusion equations, the atomic mobility in a mixture of three phases is expressed as a function of the Cr content ( $x_{\text{Cr}}$ ) and order parameters ( $\varphi_\alpha$ ) according to the characteristics of the present model.

$$M_i = M_i^{\text{A2}}(1 - p(\varphi_{\text{A2}} + \varphi_{\text{B2}})) + (M_i^{\text{A2}} \cdot p(x_{\text{Cr}}) + M_i^{\text{B2}} \cdot (1 - p(x_{\text{Cr}}))) \cdot p(\varphi_{\text{A2}} + \varphi_{\text{B2}}) \quad (28)$$

where  $p(x)$  is an interpolating monotonic polynomial.

$$p(x) = x^3(10 - 15x + 6x^2) \quad (29)$$

On the basis of Dupin's thermodynamic assessment, Campbell<sup>28</sup> developed a diffusion mobility database for A2 and B2 phases. Firstly, the atomic mobility of the A2 phase was defined in terms of absolute reaction rate theory as:<sup>34</sup>

$$M_i = M_i^0 \exp\left(\frac{-\Delta Q_i}{RT}\right) \frac{1}{RT} \quad (30)$$

where  $M_i^0$  is the frequency factor and  $M_i^0 = \sum_{\alpha} x_{\alpha} M_i^{\alpha}$  ( $\alpha = \text{Al, Cr, Ni}$ ),  $R$  is the gas constant, and  $\Delta Q_i$  is an activation energy,

which is temperature and composition-dependent.

$$\Delta Q_i = \sum_{p=1}^n x_p Q_i^p + \sum_p \sum_{q>p}^n x_p x_q \left[ \sum_{r=0}^m {}^r A_i^{pq} (x_p - x_q)^r \right] + \sum_p \sum_{q>p}^n \sum_{v>q}^n x_p x_q x_v \left[ {}^s v_{pqv}^s {}^s B_i^{pqv} \right] \quad (31)$$

where  $v_{pqv}^s = x_s + \frac{(1 - x_p - x_q - x_v)}{3}$  with  $s \in (p, q, v)$  and  ${}^r A_i^{pq}$  and  ${}^s B_i^{pqv}$  are the binary and the ternary interaction parameters, respectively.

The diffusion mobility of the B2 phase was obtained by considering an ordered ( $\Delta Q_i^{\text{ord}}$ ) contribution to the activation energy according to the thermodynamic description.

$$M_i^{\text{B2}} = M_i^0 \exp\left(\frac{-\Delta Q_i - \Delta Q_i^{\text{ord}}}{RT}\right) \frac{1}{RT} \quad (32)$$

$$\Delta Q_i^{\text{ord}} = \sum_i \sum_{i \neq j} Q_{ij}^k (y_i^{\alpha} y_j^{\beta} - x_i x_j) \quad (33)$$

where  $Q_{ij}^k$  is the contribution to the activation energy for component  $k$  as a result of the chemical ordering of the  $i$  and  $j$  atoms on the two sublattices.  $y_i^{\alpha}$  is the site fraction of component  $i$  on the  $\alpha$  sublattice that can be calculated by solving eqn (27). The mobility parameters developed by Campbell are given in Appendix A. As shown in Fig. 3, the composition dependence of the Al and Cr tracer diffusivity was obtained from the kinetic database. Note that the Al trace diffusion has a weaker composition dependence when the content of Cr is larger than 0.7. Following the work of Wang *et al.*,<sup>41</sup> the diffusion coefficients in the liquid are assumed to be  $5.0 \times 10^{-9} \text{ m}^2 \text{ s}^{-1}$ .

## 4. Thermodynamic foundation and parameters of eutectic composites

### 4.1 Thermodynamic foundation

In this work, the eutectic reaction  $\text{L} \rightarrow \text{A2} + \text{B2}$  of the Ni–33.5(at%)Al–33(at%)Cr alloy was investigated. In order to determine the model parameters quantitatively, the metastable

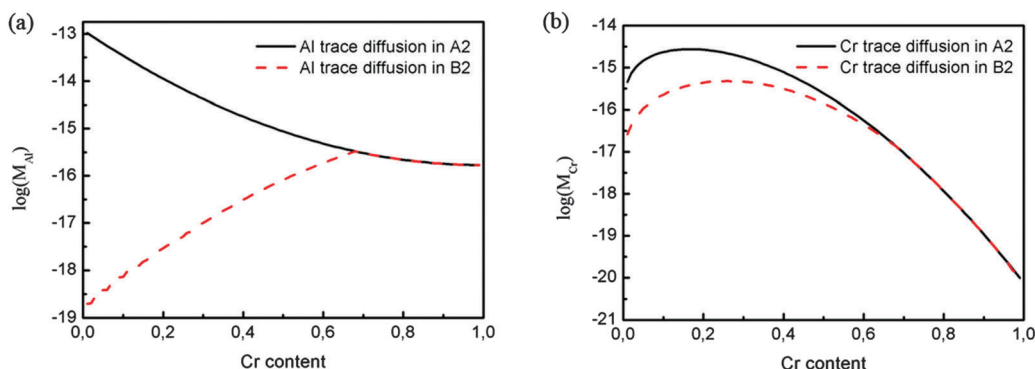


Fig. 3 Tracer diffusivity of Al (a) and Cr (b) in A2 and B2 phases as a function of mole fraction Cr at 1500 K calculated by using eqn (31) and (23) from the mobility parameters given in Appendix A.

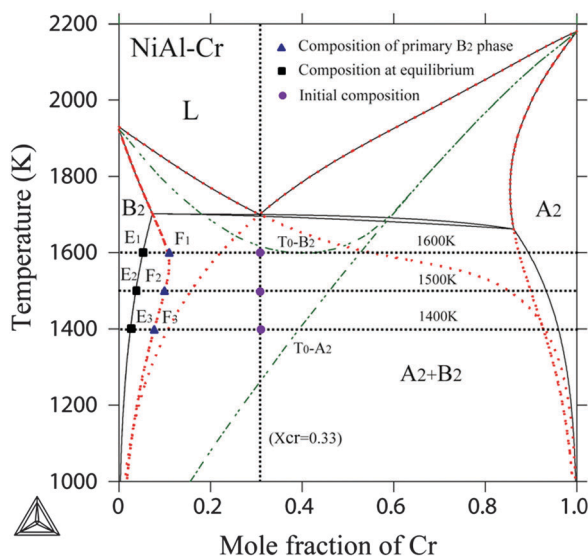


Fig. 4 Calculated NiAl–Cr phase diagram (solid lines) and metastable extensions of the solvus and liquidus curves (red dashed line). The green long-dash-dotted lines located in the two phase region represents the  $T_0$  curves of A2 and B2 phases, which are calculated according to equal Gibbs free energy for A2/L and B2/L, respectively.

extensions of the NiAl–Cr phase diagram and  $T_0$  curves were calculated, as shown in Fig. 4. The green long-dash-dotted lines represent the  $T_0$  curves, which indicate that the B2 phase will firstly nucleate from the undercooled melt by partitionless solidification because the  $T_0$ –B2 curve is higher than the  $T_0$ –A2 curve at the eutectic composition. This also can be deduced from the free energy curves as a function of Cr content shown in Fig. 5, in which the free energy of the B2 phase is more negative than that of A2 and liquid phases in the composition range of 0.0–0.6. When the eutectic alloy isothermally starts to solidify from the undercooling melt below the eutectic temperature, the composition of the primary B2 phase is assumed to be located at the metastable extension of the solvus curve (labelled by  $F_1$ ,  $F_2$  and  $F_3$  in Fig. 4) by ignoring the effect of the A2 phase

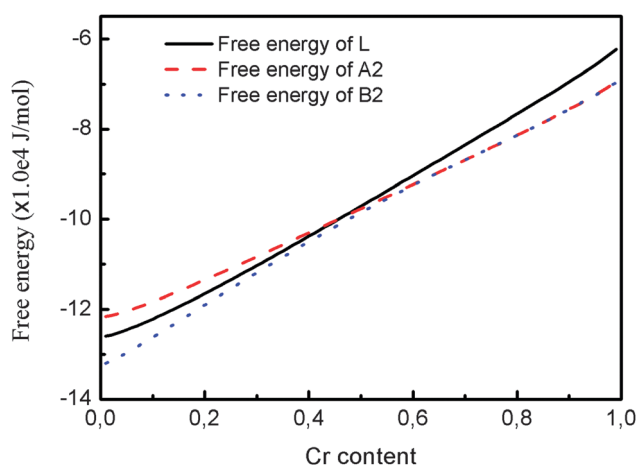


Fig. 5 Free energy of the three phases as a function of the Cr content at 1500 K.

and undercooling. Compared to the equilibrium composition marked by  $E_1$ ,  $E_2$  and  $E_3$ , the primary B2 phase is super-saturated with Cr. On the basis of the composition of the primary B2 phase given by the metastable phase diagram, the model parameters can be quantitatively determined by running numerous simulations over the large parameter space.

## 4.2 Acquiring the interfacial parameters

In this work, the gradient energy tensors, given by  $\lambda_{\alpha\beta}$  and  $k_{ij}$  coefficients, were taken to be diagonal and set as:

$$\lambda_{11} = \lambda_{22} = \lambda, \quad k_{11} = k_{22} = k \quad (34)$$

The composition gradient is related to the dependence of the alloy surface energy on composition and assumed as:

$$k = \chi_1 \cdot \lambda \quad (35)$$

where  $\chi_1 > 1$  captures the appropriate limit that the thickness of the composition interface is larger than that of the phase interface. The barrier for phase transformation in the present model is described by eqn (3), wherein  $W_{13}$  and  $W_{23}$  are the barriers for the solid–liquid interface, and  $W_{12}$  is the barrier for the solid–solid interface. According to the eutectic phase field model developed by Wheeler *et al.*,<sup>19</sup> the barrier height of the double well was suggested to be inversely proportional to the interface width and proportional to the surface energy. For simplicity, we assume that

$$W_{13} = W_{23} = \chi_2 \cdot \frac{\sigma_{sl}}{\delta} \quad (36a)$$

$$W_{12} = \chi_2 \cdot \frac{\sigma_{ss}}{\delta} \quad (36b)$$

where  $\chi_2$  is taken as a constant.  $\sigma_{sl}$  and  $\sigma_{ss}$  are the surface energies of the solid–liquid interface and the solid–solid interface, respectively. As discussed in ref. 19, it is inappropriate to take the barrier height to be inversely proportional to the interface width for solid–solid transformation. However, the solid–solid transformation is described by the diffusion equations included in the composition gradient for our thermodynamic phase field model. Therefore, the barrier for solid–solid transformation is dependent on the variation of free energy with respect to the change of composition, while  $W_{12}$  has a slight effect on the transformation.

In eqn (35)–(37), the gradient energy coefficients and barrier heights are all taken as functions of interfacial thickness and surface energy. Although the interfacial thickness was considered as a constant in most of the phase field models,<sup>42</sup> it has been well known that the interfacial thickness is temperature-dependent.<sup>43</sup> In order to obtain an appropriate composition of the primary B2 phase given by the metastable solvus curve, the interfacial thickness in the present work was taken as a function of temperature and described by an exponential decay curve.

$$\delta(T) = 4l_s \cdot T_{coe} \quad (37)$$

$$T_{coe} = y_0 + A_1 \cdot \exp(-T/A_2) \quad (38)$$

**Table 1** The materials and model parameters used for the quantitative phase field simulation

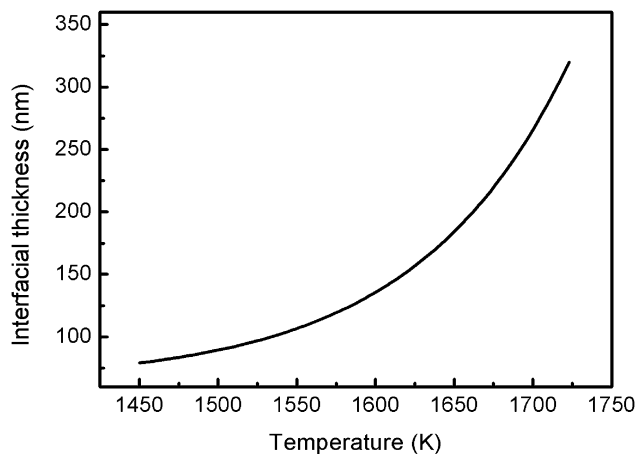
Parameters	Value
$l_s$ (m)	$2.0 \times 10^{-8}$
$l_t$ (s)	$2.0 \times 10^{-6}$
$\sigma_{ss}$ (J m <sup>-2</sup> )	0.5
$\sigma_{sl}$ (J m <sup>-2</sup> )	1.3
$M_\phi$ (m <sup>3</sup> J <sup>-1</sup> s <sup>-1</sup> )	0.0013
$V_m$ (m <sup>3</sup> mol <sup>-1</sup> )	$1.0 \times 10^{-5}$
$\chi_1$	1.29
$\chi_2$	120

where  $T_{\text{coe}}$  is the temperature coefficient of interfacial thickness.  $y_0$ ,  $A_1$  and  $A_2$  are the parameters of the exponential function. This particular exponential form is in agreement with the atomistic calculations of Frolov and Mishin, who found that the interfacial thickness is on the order of the interatomic distance at low temperatures but rapidly increases near the melting temperature.<sup>44</sup> The phase-field model parameters are listed in Table 1, while the parameters in eqn (39) were taken as  $y_0 = 0.8$ ,  $A_1 = 5.8 \times 10^{-8}$ ,  $A_2 = 96.65$ . The interfacial thickness as a function of temperature is shown in Fig. 6. It is worth noting that the composition gradient energy included together with the chemical free energy enables the variation of interfacial thickness to be tuned in the phase-field model.

### 4.3 Obtaining materials and model parameters

For the convenience of solving numerically the equations, the phase field equations are reduced to their dimensionless forms with  $x \rightarrow \Delta x \cdot l_s$  and  $t \rightarrow \tau \cdot l_t$ , where  $l_s$  and  $l_t$  are the length scale and timescale, respectively. Then, the phase field equations are nondimensionalized as follows:

$$\frac{\partial \varphi_\alpha}{\partial \tau} = -\tilde{M}_\phi \cdot \left( \frac{\partial \tilde{f}_0}{\partial \varphi_\alpha} - \sum_{\beta=1}^{N-1} \tilde{\lambda}_{\alpha\beta} \nabla^2 \varphi_\beta \right) \quad (39)$$

**Fig. 6** The change of interfacial thickness as a function of temperature.

$$\frac{\partial x_i}{\partial \tau} = \frac{l_t}{l_s^2} \cdot \nabla \cdot \left\{ [\tilde{M}_{i1}(1 - x_1) - \tilde{M}_{i2}x_1] \nabla \frac{\delta \tilde{F}}{\delta x_1} - [\tilde{M}_{i1}x_2 - \tilde{M}_{i2}(1 - x_2)] \nabla \frac{\delta \tilde{F}}{\delta x_2} \right\} \quad (40)$$

$$\frac{\delta \tilde{F}}{\delta x_i} = \sum_{\alpha=1}^3 \varphi_\alpha \frac{\partial \tilde{G}^\alpha}{\partial x_i} - \sum_{j=1}^2 \tilde{k}_{ij} \nabla^2 x_j \quad (41)$$

where  $\tilde{M}_\phi = M_\phi l_t RT / V_m$ ,  $\tilde{\lambda}_{\alpha\beta} = \lambda_{\alpha\beta} V_m / (l_s^2 RT)$ ,  $\tilde{k}_{ij} = k_{ij} V_m / (l_s^2 RT)$  and  $\tilde{G}^\alpha = G^\alpha / RT$ . We take  $\Delta x = 1$  and  $\tau_0 = 0.01$ .

In this work, the phase field equations coupled with thermodynamic and kinetic descriptions were solved using a time-adaptive pseudospectral method<sup>23,45</sup> applied to the two phase evolution equations and two diffusion equations. It should be noted that the anisotropy of gradient energy coefficients ( $\lambda_{\alpha\beta}$  and  $k_{ij}$ ) is not taken into consideration. The solidification during isothermal and continuous cooling processes was simulated based on the developed thermodynamic phase field model. For continuous cooling, as described in Appendix B, a root-finding algorithm was applied at each temperature step to obtain the six site fraction parameters and update the thermodynamic and kinetic parameters of the three phases. To save time, the root-finding algorithm was calculated at every two steps of reduced time.

## 5. Results and discussion

### 5.1 Eutectic microstructure resulting from isothermal solidification

By incorporating realistic thermo-kinetic and materials parameters of the Ni–Al–Cr ternary and invoking a variation of the liquid/solid interfacial thickness with temperature, the developed thermodynamic phase field model allows one to quantitatively simulate the process of isothermal solidification. In order to obtain the evolution details of a single eutectic cell, one critical nucleus of the B2 phase was placed at the center of a square simulation box, which corresponds to supersaturated melt with a composition of Ni–33.5%Al–33%Cr. The size of the box is  $256 \times 256$ , which is chosen to be much larger than the experimentally determined rod width and spacing. Three freezing temperatures were chosen, and the corresponding temporal evolution processes of an isolated eutectic cell are shown in Fig. 7, where the images were described by the RGB color map with  $R = x_{\text{Al}}$ ,  $G = x_{\text{Cr}}$  and  $B = x_{\text{Ni}}$ . It can be seen that the eutectic cell exhibits sunflower-like structure with fine rods. In the sunflower-like structure, the petals are enriched in Cr (in green color) and have the A2 structure, while the floret disk and inter-petals (in purple) both crystallize in the B2 structure and have the same composition. It can be apparently understood from the  $T_0$  curves in Fig. 4 that, due to the similarity of interface kinetics of A2 and B2 resulting from the cubic crystal structures, the formation of the supersaturated B2 primary phase of eutectic composition was favored over that of A2 by quenching.<sup>5</sup> It then underwent a eutectic solidification on the solidifying front into a mixture of fine rod like (A2 + B2)

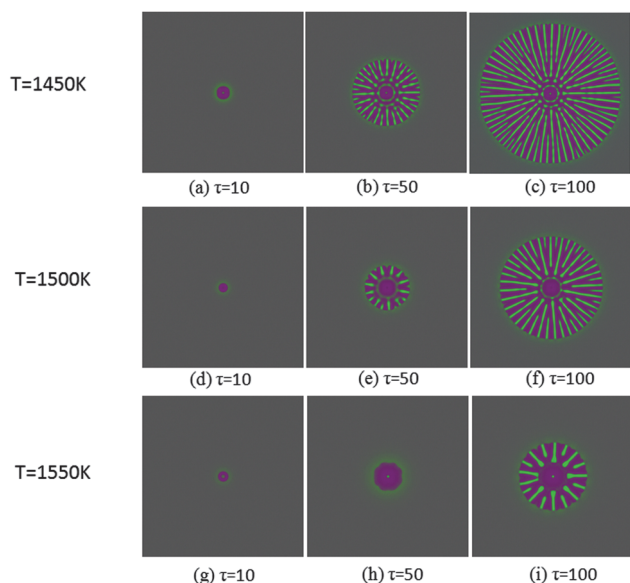


Fig. 7 Microstructural evolution process of the Ni–33.5%Al–33%Cr alloy when isothermal freezing at different temperatures. (a–c) 1450 K, (d–f) 1500 K, (g–i) 1550 K. The purple, green and gray represent the B2 phase, the A2 phase and the liquid phase, respectively.

eutectics of differing compositions. These are consistent with what were observed in Fig. 1(c) and ref. 5 and 30.

At 1450 K, the A2 rods are found to be unstable with an oscillatory pattern at the start. When the isothermal temperature increased, the stability, width, and spacing of the A2 rods increased while the growth rate of the eutectic cell decreased. Additionally, the growth of A2 rods is found to be unstable at low temperature. As shown in Table 2, the number of rods at different stages is significantly decreased with decreasing undercooling. Additionally, a Cr-rich layer was found between the primary B2 phase and lamellae. This layer has a considerable effect on the cooperative growth of A2 and B2 rods, which is detailed and discussed in Section 5.4. We also found that the nucleus would disappear if the A2 phase were taken as the initial particle. Note that the A2 phase is unstable under the mentioned conditions and cannot nucleate from the undercooling melt as the primary phase.

Continuous heterogeneous nucleation was frequently added to the phase field simulations by incorporating classical nucleation theory.<sup>46</sup> The circular nuclei of A2 and B2 phases were introduced at the random locations with a constant nucleation attempt rate. The radius of the particle was calculated

according to classical theory for nucleation energy,<sup>41</sup> in which the free energy difference between A2(B2) and L was quantitatively evaluated. Fig. 8 shows transformation kinetics and morphological evolution during the isothermal solidification process at 1500 K. The simulations were performed in a square box  $512 \times 512$  with periodic boundary conditions. As shown in Fig. 8(a), the transformation curves can be divided into three stages. In the first stage, the nuclei of the B2 phase with different sizes are found randomly embedded in the matrix while the nuclei of the A2 phase chooses to disappear (Fig. 8(b)). In the second stage, the transformations with concurrent nucleation and growth took place (Fig. 8(c)). It becomes evident in Fig. 8 that the nucleation and growth of the A2 rods occur by a process of secondary or growth front nucleation, *i.e.* at the perimeter of the growing primary B2 disk at this stage (Fig. 8(d)). In the third stage, the liquid phase vanished and solidification completed, and the microstructure experiences complex transformations involving CSD and coarsening (Fig. 8(e)). Besides, the microstructure with continuous heterogeneous nucleation of the B2 phase shown in Fig. 8(e) is in good agreement with the experimental microstructure in cast NiAl–Cr(Mo) near eutectic alloys (Fig. 1 and 3 of ref. 31).

The Cr atoms in the supersaturated B2 rods have a great tendency to diffuse uphill into the A2 rods, leading to the coarsening of the A2 phase, while the primary B2 phase, meeting all requirements of CSD, will undergo a CSD transformation into a mixture of disordered A2 and ordered B2. However, the CSD domains, which have been confirmed by experiments,<sup>5</sup> are not covered in the present simulations due to the timescale and length scale limits. As observed in ref. 5 and 24, spinodal decomposition results in an ultra fine scale compositional separation. Fig. 9 shows the transformation kinetics obtained at different isothermal temperatures. Although the transformation takes place more quickly at lower temperatures, the increase of the transformation rate is not proportional to the temperature difference. As shown in Fig. 9, the difference in kinetics among 1400 K, 1450 K and 1500 K is much smaller than that involving 1550 K, possibly due to the saturated and stable nucleation below 1500 K. Additionally, a minor difference in the final fraction of the B2 phase can also be observed in the transformation curves, and reveals that high solidification temperature benefits the growth of the A2 phase. It is noteworthy that the numerical results have a good agreement with the experimental findings, which emphasize an increase of the width of A2 rods, rod spacing and size of primary B2 particles at high solidification temperature.

## 5.2 Microstructure evolution during cooling

In this section, the eutectic solidification during cooling is simulated by using a near equilibrium assumption. As described by eqn (2), the free energy dependence on  $\nabla c$  is important for rapid solidification because it captures the solute trapping effect. The simulations start from 1600 K and  $x_{\text{Cr}} = 0.33$ , *i.e.* meaning that the eutectic alloy was cooled from 1600 K with different cooling rates. It was performed at a square domain of  $512 \times 512$  grid points, and the continuous

Table 2 Morphology parameters obtained from the simulation of the isolated cell

Temperature (K)	Number			Reference state
	Primary rods	Secondary rods	Tertiary rods	
1450	18	17	30	$\tau = 100$
1500	13	12	25	$\tau = 140$
1550	9	9	16	$\tau = 180$



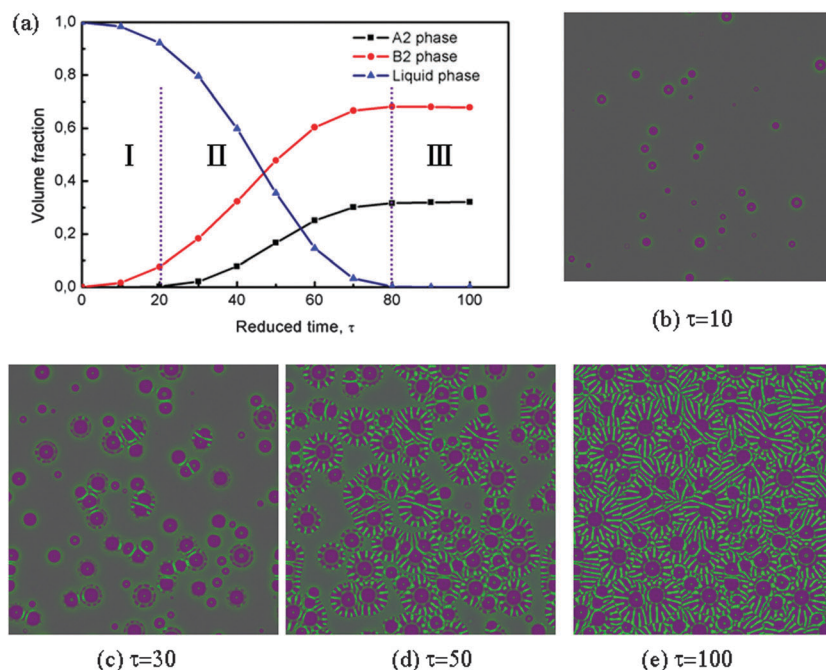


Fig. 8 Transformation kinetics (a) and microstructural changes (b–e) obtained from the phase field simulation in the case of continuous nucleation when isothermal freezing at 1500 K.

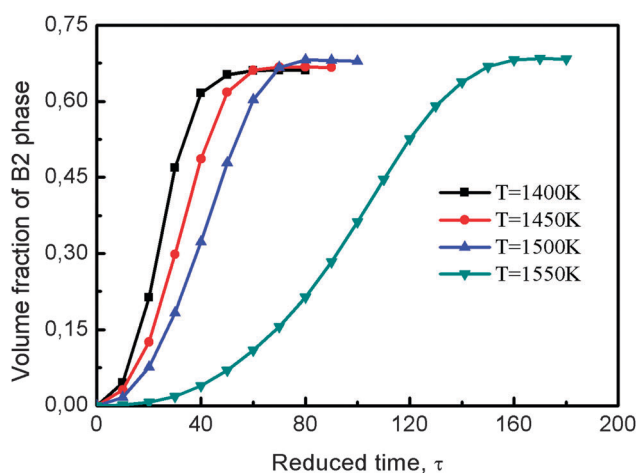


Fig. 9 The transformation kinetics obtained at different isothermal temperatures.

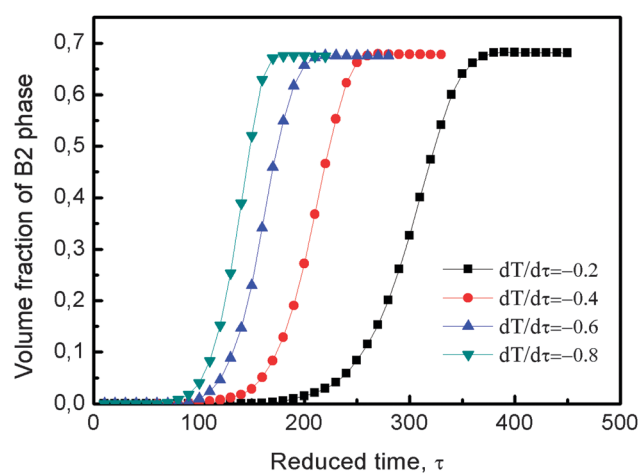


Fig. 10 The transformation kinetics of the B2 phase obtained at different cooling rates.

nucleation event described in Section 5.1 was added to the model as well. After every nucleation event, the growth or disappearance of the nuclei is determined by the competition between local chemical driving force and the resistance induced by interfacial energy. Therefore, most of the nuclei choose to disappear at the initial state of the simulation due to the fact that 1600 K is very close to the  $T_0$  curve of the B2 phase (shown in Fig. 4). Fig. 10 shows the transformation kinetics of the B2 phase obtained at different cooling rates. When the system temperature decreases to below the  $T_0$  curve, the nuclei of the B2 phase become stable and grow with time because the Cr composition is gradually enriched around the primary B2

phase, and then the A2 phase grows from the boundary of the B2 particles. The real temperature and time for the nucleation of A2 rods can be simply evaluated by the intersection point between the  $T_0$  curve of the A2 phase (shown in Fig. 4) and composition around the B2 particles. As shown in Fig. 10, the transformation rate changes linearly with increasing cooling rates.

The effect of the cooling rate on the resulting microstructure is shown in Fig. 11. It is clear that the size of the eutectic cell monotonically increases as the cooling rate decreases. Although the average size of the B2 particles increases with decreasing cooling rate, we can see from Fig. 11 that it does not

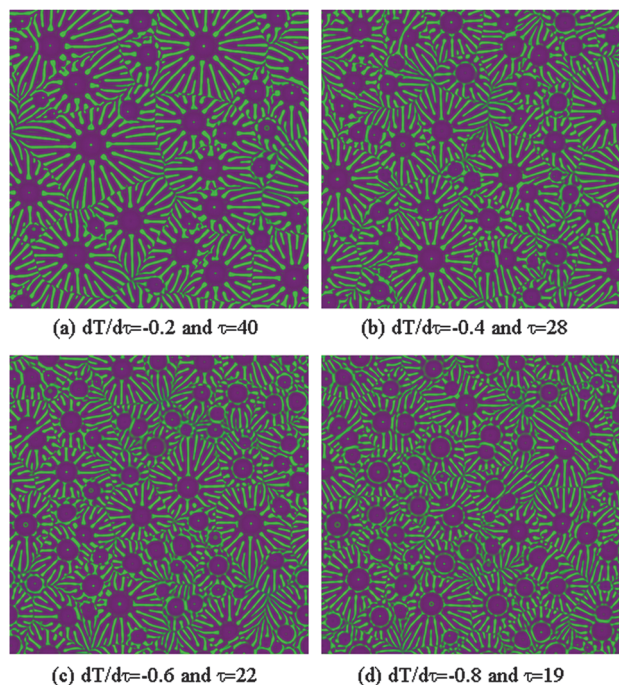


Fig. 11 Microstructures obtained after complete solidification for various cooling rates. The size of the domain is  $10.24 \mu\text{m} \times 10.24 \mu\text{m}$ .

increase as rapidly as the eutectic cell size. Besides, the Cr-rich layer around the primary B2 phase is found to be converted to ring distributed nuclei due to the increasing degree of segregation. For the variational interfacial thickness proposed in the present model, the solute trapping effect will be enhanced in the cooling process, contributing to the segregation around the primary B2 particles.

From this point of view, the variation of interfacial thickness with temperature is responsible for the formation of an enriched layer at the solidification front that affects the nucleation of A2 rods and the morphology of the eutectic structure. However, the primary B2 particles produced at different cooling rates almost have the same composition, as shown in Fig. 12. It reveals that the cooling rate has little effect on the composition of B2 particles. It is important to note that the composition peak in the center of the B2 particle is induced by the initial nucleus and the position variation at the right ends shown in Fig. 12 and similarly induced by the size difference between the B2 particles.

### 5.3 Formation mechanism of the eutectic structure in NiAl–Cr composites

As demonstrated by thermodynamic prediction, experimental, and simulation results, the B2 phase with supersaturated Cr first nucleates from the undercooled melt. With increasing solidification temperature or decreasing cooling rate, the size of primary B2 disks increases due to the decrease of the driving force for the formation of A2 phase. However, the effect of solute trapping increases as the solidification temperature increases (the interface velocity decreases) resulting in a larger A2 nucleus at the outer boundary of B2 disks. With the isotropic interfacial condition, the lamellae grow as spherical B2 particles

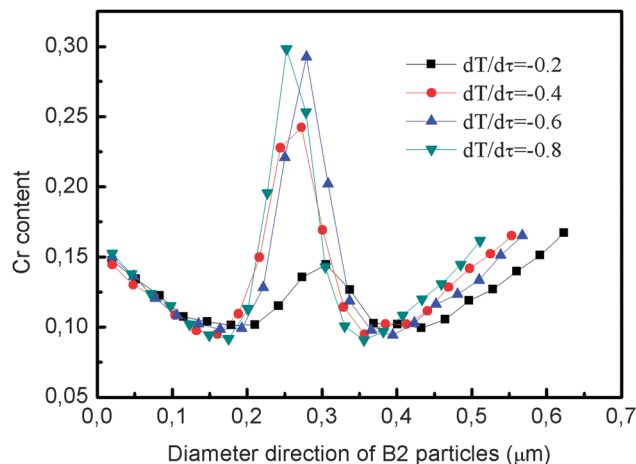


Fig. 12 Profile of Cr content through primary B2 particles for different cooling rates. Note that the four B2 particles with different diameters are selected randomly.

with supersaturated Cr in a radial manner, which has been found in many multicomponent near-eutectic composites<sup>30,47,48</sup> except for NiAl based composites.<sup>49–51</sup> As discussed above, the A2 rods have been found to nucleate from the Cr-rich layer around the primary B2 phase, and then grow to form alternated A2 and B2 rods. As the rods grow, the B2 rods become unstable due to the increase of width and then the interface shape will transform from convex to concave, at the center of which the secondary A2 rods nucleate and grow perpendicular to the solidification front. This feature has been confirmed by experiments and analysis models.<sup>18,52</sup>

The Cr-rich layer continues to evolve after solidification, driven by the composition difference between the equilibrium state and local positions. Fig. 13 shows the composition evolution process of the two special positions in the Cr-rich layer and

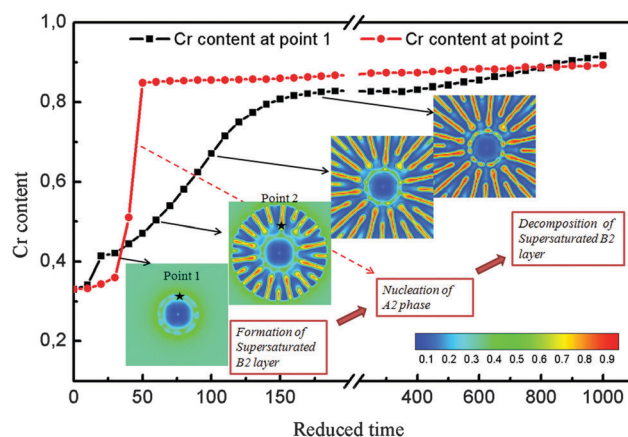


Fig. 13 The composition of two special points in the B2 ribbon (around the primary B2 particle) and A2 rods as a function of time for isothermal solidification at 1500 K. The coordinates of the two points are (130, 145) and (130, 155), as labeled by 5-Point Star in insets. It is worth to note that the insets are mapped as a function of Cr content to get a clear observation of the B2 ribbon, and the contour legend is shown at the bottom of insets.



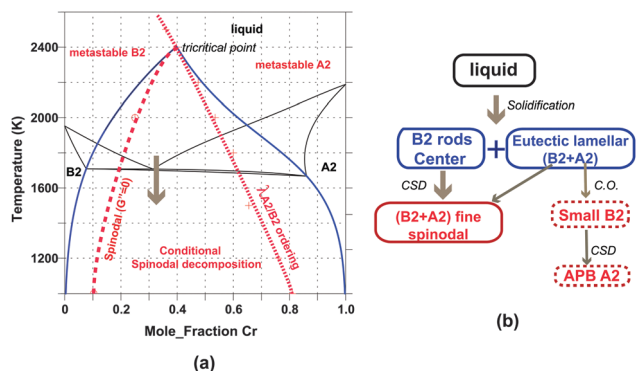


Fig. 14 (a) The NiAl–Cr phase diagram depicting conditional spinodal decomposition; (b) the transformation (reaction) paths of the NiAl–33at%Cr alloy involving conditional spinodal contingent on prior ordering.

A2 rod, respectively. It can be observed from Fig. 13 that the Cr content at point 2 experiences a jump at  $\tau = 30\text{--}40$  indicating the formation of A2 rods from undercooled melt, while the Cr content at the Cr-rich layer (labelled by point 1) changes gradually as a S-shape indicating a diffusion controlled process. The formation and evolution of the Cr-rich layer around the primary B2 particles can be observed clearly. It is important to note that the Cr-rich layer will convert to ring distributed nuclei from which the A2 rods grow up perpendicular to the solidification front.

The conditional spinodal decomposition of the NiAl–Cr system was calculated by suspending the liquid phase (thus a metastable extension at high temperatures) under a rapidly solidified nonequilibrium condition, as shown in Fig. 14(a). It becomes evident that the continuous CSD occurs in such a region (red) bounded by the spinodal line (red dashed, the limit to metastability of B2) and the continuous A2/B2 order transitions (red dotted), as well as their metastable extension and intersection indeed at a tricritical point (39.8 at%, 2403 K). Recalling also the simulation results before, the formation process of eutectic structure can be envisioned in the following sequence by six steps in Fig. 15:

(I) The supersaturated B2 phases nucleate from undercooled melt by partitionless solidification and grow as single-phase B2 disks with a large homogeneous domain (Fig. 15(a));

(II) The buildup of the Cr-rich layer in the solidification front due to the rejection of Cr at the interface of the primary B2 disk, as noted by the pink ribbon in Fig. 15(b);

(III) The enriched regions starts to evolve into more Cr-enriched parts and Cr-lean parts, and they act as high-energy sites that aid in nucleating the secondary B2 phases in rods at the Cr-lean sites of the ribbon while the A2 rods near the Cr-enriched sites (Fig. 15(c)).

(IV) The eutectic structures consisting of alternating A2 and B2 rods grow up perpendicular to the local orientation of the solidification front, thus forming a radial pattern (Fig. 15(d));

(V) The eutectic cell tends to keep a fixed lamellar spacing by creating secondary, tertiary (*etc.*) rods (Fig. 15(e));

(VI) As the solidification completes, the Cr atoms keep transporting from B2 rods to A2 rods until the equilibrium

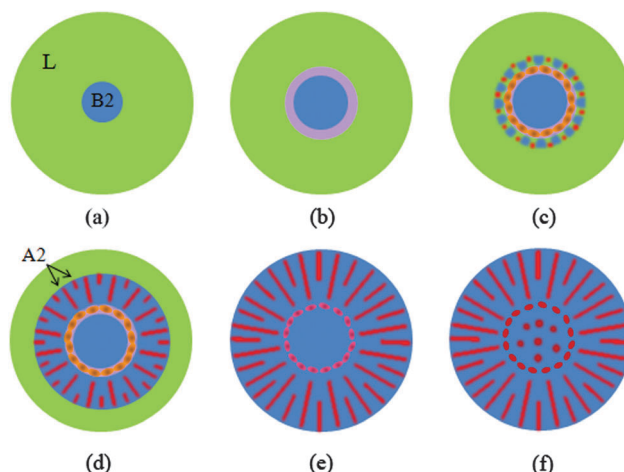


Fig. 15 The formation mechanism of the sunflower-like eutectic structure in NiAl–Cr composites.

composition is reached, meanwhile, the large supersaturated primary B2 disk is about to become unstable with respect to composition variation, thus undergoing a CSD and transforming into more stable fine (B2 + A2) seed-like domains (Fig. 15(f)) with composition near the eutectics. This observation was clearly made by us on the solidified NiAl–Cr(W) alloy (as shown in Fig. 16) and on  $\text{Al}_2\text{CrCuFeNi}_2$  (Fig. 1b of ref. 30).

Although our simulations and experiments do not explicitly test the microstructures developed at finer scales at lower CSD temperatures, *i.e.* the dashed boxes in Fig. 14(b), we still infer further that, well within the CSD and beginning from the A2 phase of the eutectics, most transformations in the NiAl–33at%Cr alloy involve B2 continuous ordering, leading to a fine-domain B2 structure. This fine B2 state is unstable with respect to phase separation, by a segregation of Cr to the antiphase boundary of small B2 enhanced by uphill diffusion, the alloy undergoes a spinodal reaction, thus finally forming a continuous layer of A2 on the APBs of B2 as indicated by the dashed-boxes in Fig. 14(b).

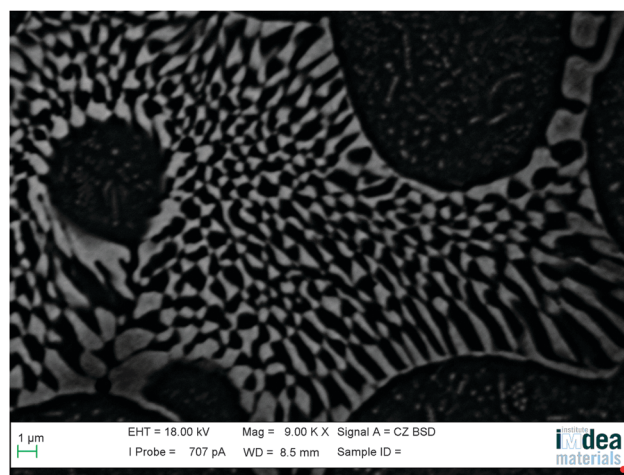


Fig. 16 Sunflower-like eutectic structure in NiAl–Cr alloys obtained by experiment.

However, these morphologies are only visualizable at the scale of the wavelength of concentration waves on the nanoscale.

## 6. Conclusion

In the present work, we developed a thermodynamic phase field model to describe the nonequilibrium formation of eutectic structures in ternary NiAl–Cr alloys, with real thermodynamic and materials parameters integrated into the model. In a spirit of the CALPHAD methodology, the Gibbs free energies of disordered A2 and ordered B2 phases were expressed by a single formalism, so were treated the mobilities of the two phases with an extra chemical ordering contribution. The model was implemented with a variation of the liquid/solid interfacial thickness with temperature. The subsequent modeling was thoroughly performed to simulate the microstructures resulting from the solidification under isothermal and continuous cooling conditions. The simulated eutectic structures exhibit a sunflower-like pattern consisting of the (A2 + B2) eutectic lamellae (*i.e.* the A2 and B2 petals) embedded in the primary B2 cell disk (*i.e.* florets), consistent with experimental observations.

Together with the thermodynamically predicted NiAl–Cr pseudo-binary system that includes conditional spinodal decomposition (*i.e.* spinodal decomposition occurs only if B2 orders first),

the mechanism that governs the formation of the peculiar eutectic morphology was envisioned from the modeled evolutions and described in six sequential steps. Our calculation suggests that CSD occurrence in sequence could further revise the microstructure of the eutectics by generating fine-domain structures, thereby providing an additional method to explore the novel NiAl-based eutectic composites with tunable properties at elevated temperatures.

## Appendix A: thermodynamic and kinetic databases of the NiAl–Cr system

The CALPHAD description of the Gibbs energies and mobilities for Liquid, A2 and B2 phases is given in Table 3, according to the assessment results derived by Dupin<sup>27</sup> and Campbell<sup>28</sup> and removing the effect of vacancy. The thermodynamic and kinetic models of disordered A2 and ordered B2 phases are shown in eqn (18), (23), (31) and (33). The reference free energy parameters of pure elements, *i.e.*  ${}^0G_{\text{m,Al}}$ ,  ${}^0G_{\text{m,Cr}}$  and  ${}^0G_{\text{m,Ni}}$ , were given by the SGTE database in ref. 40. In Table 3, the parameters  $\alpha$  and  $\lambda$  have the following forms:  $\alpha = -152\,397 + 26.41T$ ,  $\lambda = -52\,441 + 11.30T$ . Besides, the free energy is expressed in J mol<sup>−1</sup> and temperature  $T$  is given in K.

Table 3 Thermodynamic and mobility parameters for the liquid, A2 and B2 phases of NiAl–Cr system

Type		Liquid phase	A2 phase	B2 phase
Thermodynamic database	$L_{\text{Al,Cr}}^{\phi}$	${}^0L_{\text{Al,Cr}}^{\phi}: -2.9 \times 10^4$ ${}^1L_{\text{Al,Cr}}^{\phi}: -1.1 \times 10^4$	${}^0L_{\text{Al,Cr}}^{\phi}: -5.49 \times 10^4 + 10T$	—
	$L_{\text{Al,Ni}}^{\phi}$	${}^0L_{\text{Al,Ni}}^{\phi}: -2.07 \times 10^5 + 41.32T$ ${}^1L_{\text{Al,Ni}}^{\phi}: -1.02 \times 10^4 + 5.87T$ ${}^2L_{\text{Al,Ni}}^{\phi}: 8.12 \times 10^4 - 31.96T$ ${}^3L_{\text{Al,Ni}}^{\phi}: 4.37 \times 10^3 - 2.52T$ ${}^4L_{\text{Al,Ni}}^{\phi}: -2.21 \times 10^4 + 13.16T$	${}^0L_{\text{Al,Ni}}^{\phi}: -2.05 \times 10^5 + 37.71T$	—
	$L_{\text{Cr,Ni}}^{\phi}$	${}^0L_{\text{Cr,Ni}}^{\phi}: 3.18 \times 10^2 - 7.33T$ ${}^1L_{\text{Cr,Ni}}^{\phi}: 1.69 \times 10^4 - 6.37T$	${}^0L_{\text{Cr,Ni}}^{\phi}: 17\,170 - 11.82T$ ${}^1L_{\text{Cr,Ni}}^{\phi}: 34\,418 - 11.86T$	—
	$L_{\text{Al,Cr,Ni}}^{\phi}$	$1.6 \times 10^4$	$4.25 \times 10^4$	—
	$G_{\text{Al,Cr}}^{\bullet\text{B2}}$	—	—	$-2.0 \times 10^3$
	$G_{\text{Al,Ni}}^{\bullet\text{B2}}$	—	—	$0.5\alpha - 0.5\lambda$
	$G_{\text{Cr,Ni}}^{\bullet\text{B2}}$	—	—	$4.0 \times 10^3$
	$Q_{\text{Al}}^{\text{p}}$	—	$Q_{\text{Al}}^{\text{Al}} = Q_{\text{Cr}}^{\text{Cr}} = Q_{\text{Ni}}^{\text{Ni}}: -2.15 \times 10^5$	—
	$Q_{\text{Cr}}^{\text{p}}$	—	$Q_{\text{Cr}}^{\text{Al}} = Q_{\text{Cr}}^{\text{Ni}}: -2.18 \times 10^5$ $Q_{\text{Cr}}^{\text{Cr}}: -4.07 \times 10^5$	—
	$Q_{\text{Ni}}^{\text{p}}$	—	$Q_{\text{Ni}}^{\text{Al}} = Q_{\text{Ni}}^{\text{Cr}}: -2.04 \times 10^5$ $Q_{\text{Ni}}^{\text{Cr}}: -4.07 \times 10^5$	—
Kinetic database	${}^0A_{\text{Al,Ni}}^{\text{Al}}$	—	$3.27 \times 10^5$	—
	${}^0A_{\text{Al,Ni}}^{\text{Ni}}$	—	$3.27 \times 10^5$	—
	${}^0A_{\text{Cr,Ni}}^{\text{Al}}$	—	$3.5 \times 10^5$	—
	${}^0A_{\text{Cr,Ni}}^{\text{Ni}}$	—	$3.5 \times 10^5$	—
	$Q_{\text{ij}}^{\text{Al}}$	—	—	$Q_{\text{Al,Ni}}^{\text{Al}} = Q_{\text{Al,Cr}}^{\text{Al}}: -3.46 \times 10^5$ $Q_{\text{Cr,Ni}}^{\text{Al}}: -9.19 \times 10^5$ $Q_{\text{Al,Cr}}^{\text{Cr}}: -3.19 \times 10^5$ $Q_{\text{Al,Ni}}^{\text{Cr}}: -7.43 \times 10^4$ $Q_{\text{Cr,Ni}}^{\text{Cr}}: -3.9 \times 10^5$ $Q_{\text{Al,Ni}}^{\text{Ni}} = Q_{\text{Al,Cr}}^{\text{Ni}}: -3.19 \times 10^5$ $Q_{\text{Cr,Ni}}^{\text{Ni}}: -3.90 \times 10^5$
	$Q_{\text{ij}}^{\text{Cr}}$	—	—	
	$Q_{\text{ij}}^{\text{Ni}}$	—	—	
	${}^0A_{\text{Al,Ni}}^{\text{Al}}$	—		
	${}^0A_{\text{Al,Ni}}^{\text{Ni}}$	—		
	${}^0A_{\text{Cr,Ni}}^{\text{Al}}$	—		



## Appendix B: thermodynamic modeling of the ordered B2 phase in NiAl–Cr composites

For a ternary alloy composed of Al, Cr and Ni, the thermodynamic modeling of the ordered B2 phase was described by the MSL formalism  $(\text{Al,Cr,Ni})_{0.5}(\text{Al,Cr,Ni})_{0.5}$ . In the MSL model, the site fractions and mole fractions must follow three conditions: (1) the fractional occupancies over two SL for each alloying element must be equal to the mole fraction of that element, (2) the sum of the fractional occupancies in each SL must be equal to 1, (3) the sum of the mole fractions must equal 1.

$$\frac{1}{2} \sum_{s=1}^2 y_i^{(s)}(\mathbf{r}, t) = x_i(\mathbf{r}, t) \quad i = 1, 2, 3 \quad (\text{B1})$$

$$\sum_{i=1}^3 y_i^{(s)}(\mathbf{r}, t) = 1 \quad s = 1, 2 \quad (\text{B2})$$

$$\sum_{i=1}^3 x_i(\mathbf{r}, t) = 1 \quad (\text{B3})$$

By considering the definition equations of the departure degree and long-range order degree, eqn (26), the six site fractions can be written as a function of  $(\theta_1, \theta_2, \sigma_1, \sigma_2)$ .

$$y_1' = \frac{1 + \theta_1 + \sigma_1}{2} \quad (\text{B4})$$

$$y_1'' = \frac{1 + \theta_1 - \sigma_1}{2} \quad (\text{B5})$$

$$y_2' = \frac{-\theta_1 - \theta_2 - \sigma_1 - \sigma_2}{2} \quad (\text{B6})$$

$$y_2'' = \frac{-\theta_1 - \theta_2 + \sigma_1 + \sigma_2}{2} \quad (\text{B7})$$

$$y_3' = \frac{1 + \theta_2 + \sigma_2}{2} \quad (\text{B8})$$

$$y_3'' = \frac{1 + \theta_2 - \sigma_2}{2} \quad (\text{B9})$$

where the range of  $\theta_1, \theta_2, \sigma_1$  and  $\sigma_2$  can be determined according to the intrinsic limitation of  $x_i$  and  $y_i^{(s)}$ , i.e.  $0 \leq x_i \leq 1$  and  $0 \leq y_i^{(s)} \leq 1$ . The range of  $\theta_1, \theta_2, \sigma_1$  and  $\sigma_2$  locates in the shadow area in Fig. 17.

According to eqn (26), we can get that

$$\frac{\partial \theta_1}{\partial x_1} = 2, \quad \frac{\partial \theta_1}{\partial x_2} = 0 \quad (\text{B10})$$

$$\frac{\partial \theta_2}{\partial x_1} = -2, \quad \frac{\partial \theta_2}{\partial x_2} = -2 \quad (\text{B11})$$

$$\frac{\partial \sigma_1}{\partial x_1} = 2 \cdot \frac{\partial \sigma_1}{\partial \theta_1} - 2 \cdot \frac{\partial \sigma_1}{\partial \theta_2}, \quad \frac{\partial \sigma_1}{\partial x_2} = -2 \cdot \frac{\partial \sigma_1}{\partial \theta_2} \quad (\text{B12})$$

$$\frac{\partial \sigma_2}{\partial x_1} = 2 \cdot \frac{\partial \sigma_2}{\partial \theta_1} - 2 \cdot \frac{\partial \sigma_2}{\partial \theta_2}, \quad \frac{\partial \sigma_2}{\partial x_2} = -2 \cdot \frac{\partial \sigma_2}{\partial \theta_2} \quad (\text{B13})$$

Therefore, the derivative of  $y_i^{(s)}$  with respect to composition  $x_i$  is given by:

$$\frac{\partial y_1'}{\partial x_1} = 1 + \frac{\partial \sigma_1}{\partial \theta_1} - \frac{\partial \sigma_1}{\partial \theta_2}, \quad \frac{\partial y_1'}{\partial x_2} = -\frac{\partial \sigma_1}{\partial \theta_2} \quad (\text{B14})$$

$$\frac{\partial y_1''}{\partial x_1} = 1 - \frac{\partial \sigma_1}{\partial \theta_1} + \frac{\partial \sigma_1}{\partial \theta_2}, \quad \frac{\partial y_1''}{\partial x_2} = \frac{\partial \sigma_1}{\partial \theta_2} \quad (\text{B15})$$

$$\frac{\partial y_2'}{\partial x_1} = -\left(\frac{\partial \sigma_1}{\partial \theta_1} - \frac{\partial \sigma_1}{\partial \theta_2} + \frac{\partial \sigma_2}{\partial \theta_1} - \frac{\partial \sigma_2}{\partial \theta_2}\right), \quad (\text{B16})$$

$$\frac{\partial y_2'}{\partial x_2} = 1 + \frac{\partial \sigma_1}{\partial \theta_2} + \frac{\partial \sigma_2}{\partial \theta_2}$$

$$\frac{\partial y_2''}{\partial x_1} = \frac{\partial \sigma_1}{\partial \theta_1} - \frac{\partial \sigma_1}{\partial \theta_2} + \frac{\partial \sigma_2}{\partial \theta_1} - \frac{\partial \sigma_2}{\partial \theta_2}, \quad (\text{B17})$$

$$\frac{\partial y_2''}{\partial x_2} = 1 - \frac{\partial \sigma_1}{\partial \theta_2} - \frac{\partial \sigma_2}{\partial \theta_2}$$

$$\frac{\partial y_3'}{\partial x_2} = -1 - \frac{\partial \sigma_2}{\partial \theta_2} \quad (\text{B18})$$

$$\frac{\partial y_3''}{\partial x_1} = -1 - \frac{\partial \sigma_2}{\partial \theta_1} + \frac{\partial \sigma_2}{\partial \theta_2}, \quad \frac{\partial y_3''}{\partial x_2} = -1 + \frac{\partial \sigma_2}{\partial \theta_2} \quad (\text{B19})$$

Using eqn (27), the  $(\sigma_1, \sigma_2)$  at a certain composition and temperature can be calculated using a root-finding algorithm.

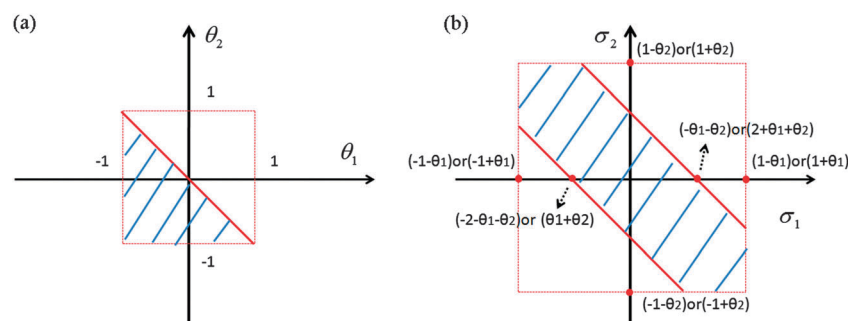


Fig. 17 The range of  $\theta_1, \theta_2, \sigma_1$  and  $\sigma_2$ .

We take  $\sigma_i$  as a function of  $\theta_i$  and it is numerically calculated by the central difference method.

## Acknowledgements

The authors want to acknowledge “AMAROUT II EUROPE” Marie Curie COFUND action, partially funded by the European Union’s 7th Framework Programme under Grant Agreement no. 291803. This work also supported by the “111” Project (No. B08040). S. M. acknowledges funding of the Project NECTAR (PCIG10-GA-2011-303409) by the Marie Curie Actions Grant FP7-PEOPLE-2011-CIG Programme.

## References

- 1 R. Darolia, *J. Mater. Sci. Technol.*, 1994, **10**, 157.
- 2 I. E. Locci, R. M. Dickerson, A. Grag, R. D. Noebe, J. D. Whittenberger, M. V. Nathal and R. Darolia, *J. Mater. Res.*, 1996, **11**, 3024.
- 3 K. W. Huai, J. T. Guo, Z. R. Ren, Q. Gao and R. Yang, *J. Mater. Sci. Technol.*, 2006, **22**, 164.
- 4 D. B. Miracle, *Acta Mater.*, 1993, **41**, 649.
- 5 D. Shechtman, W. J. Boettinger and T. Z. Kattamis, *Acta Metall.*, 1984, **32**, 749.
- 6 D. Frankel, S. Milenkovic, A. J. Smith and A. W. Hassel, *Electrochim. Acta*, 2009, **54**, 6015.
- 7 S. Milenkovic and R. Caram, *J. Mater. Process. Technol.*, 2003, **143–144**, 629.
- 8 S. Milenkovic, A. Schneider and G. Frommeyer, *Intermetallics*, 2011, **19**, 342.
- 9 L. Y. Sheng, J. T. Guo and H. Q. Ye, *Mater. Des.*, 2009, **30**, 964.
- 10 R. I. Barabash, W. Liu, J. Z. Tischler, H. Bei and J. D. Budai, *Acta Mater.*, 2012, **60**, 3279.
- 11 Y. H. Wen, J. V. Lill, S. L. Chen and J. P. Simmons, *Acta Mater.*, 2010, **58**, 875.
- 12 J.-L. Fattebert, M. E. Wickett and P. E. A. Turchi, *Acta Mater.*, 2014, **62**, 89.
- 13 I. Steinbach and F. Pezzolla, *Phys. D*, 1999, **134**, 385.
- 14 I. Steinbach, F. Pezzolla, B. Nestler, M. Seeßelberg, R. Prieler, G. J. Schmitz and J. L. L. Rezende, *Phys. D*, 1996, **94**, 135.
- 15 I. Steinbach and M. Apel, *Phys. D*, 2006, **217**, 153.
- 16 J. Kundin, R. Kumar, A. Schlieter, M. A. Choudhary, T. Gemming, U. Kühn, J. Eckert and H. Emmerich, *Comput. Mater. Sci.*, 2012, **63**, 319.
- 17 F. Drolet, K. R. Elder, M. Grant and J. M. Kosterlitz, *Phys. Rev. E: Stat. Phys., Plasmas, Fluids, Relat. Interdiscip. Top.*, 2000, **61**, 6705.
- 18 Z. Ebrahimi, J. L. Rezende and J. Kundin, *J. Cryst. Growth*, 2012, **349**, 36.
- 19 A. A. Wheeler, G. B. McFadden and W. J. Boettinger, *Proc. R. Soc. Lond. A*, 1996, **452**, 495.
- 20 B. Nestler and A. A. Wheeler, *Phys. D*, 2000, **138**, 114.
- 21 A. A. Wheeler, W. J. Boettinger and G. B. McFadden, *Phys. Rev. E: Stat. Phys., Plasmas, Fluids, Relat. Interdiscip. Top.*, 1993, **47**, 1893.
- 22 D. J. Seol, S. Y. Hu, Y. L. Li, J. Shen, K. H. Oh and L. Q. Chen, *Acta Mater.*, 2003, **51**, 5173.
- 23 D. A. Cogswell and W. Craig Carter, *Phys. Rev. E: Stat., Nonlinear, Soft Matter Phys.*, 2011, **83**, 061602.
- 24 S. M. Allen and J. W. Cahn, *Acta Metall.*, 1976, **24**, 425.
- 25 W. A. Soffa and D. E. Laughlin, *Proceedings of an International Conference on Solid-Solid Phase Transformations*, AIME, Pittsburgh, 1982.
- 26 R. D. Noebe and W. S. Walston, *Structural intermetallics*, Minerals, Metals & Materials Society, Warrendale, 1996.
- 27 N. Dupin, I. Ansara and B. Sundman, *Calphad*, 2001, **25**, 279.
- 28 C. E. Campbell, *Acta Mater.*, 2008, **56**, 4277.
- 29 H. E. Cline and J. L. Walter, *Met. Trans.*, 1970, **1**, 2907.
- 30 S. Guo, C. Ng and C. T. Liu, *Mater. Res. Lett.*, 2013, **1**, 228.
- 31 L. Y. Sheng, W. Zhang, J. T. Guo and H. Q. Ye, *Mater. Charact.*, 2009, **60**, 1311.
- 32 S. M. Allen and J. W. Cahn, *Acta Metall.*, 1979, **27**, 1085.
- 33 S. Emmanuel, A. Cortis and B. Berkowitz, *Chem. Phys.*, 2004, **302**, 21.
- 34 J. O. Andersson and J. Agren, *J. Appl. Phys.*, 1992, **72**, 1350.
- 35 K. Wu, J. E. Morral and Y. Wang, *Acta Mater.*, 2004, **52**, 1917.
- 36 N. Saunders and A. P. Miodownik, *CALPHAD (calculation of phase diagrams): a comprehensive guide*, Pergamon Press, Oxford, 1998.
- 37 O. Redlich and A. Kister, *Ind. Eng. Chem.*, 1948, **40**, 345.
- 38 N. Dupin, PhD thesis, Institut National Polytechnique de Grenoble, 1995.
- 39 N. Dupin and I. Ansara, *Z. Metallkd.*, 1999, **90**, 76.
- 40 A. T. Dinsdale, *Calphad*, 1991, **15**, 317.
- 41 W. Y. Wang, H. Z. Fang, S. L. Shang, H. Zhang, Y. Wang, X. Hui, S. Mathaudhu and Z. K. Liu, *Physica B*, 2011, **406**, 3089.
- 42 A. A. Wheeler, W. J. Boettinger and G. B. McFadden, *Phys. Rev. A: At., Mol., Opt. Phys.*, 1992, **45**, 7424.
- 43 A. J. Ardell, *Scr. Mater.*, 2012, **66**, 423.
- 44 T. Frolov and Y. Mishin, *Phys. Rev. B: Condens. Matter Mater. Phys.*, 2009, **79**, 045430.
- 45 D. A. Cogswell, PhD thesis, Massachusetts Institute of Technology, 2010.
- 46 R. W. Balluffi, S. M. Allen and W. Craig Carter, *Kinetics of materials*, John Wiley & Sons Inc., Hoboken, 2005.
- 47 Y. N. Taran and V. M. Snagovskii, *Met. Sci. Heat Treat.*, 1966, **8**, 27.
- 48 M. Timpel, N. Wanderka, R. Grothausmann and J. Banhart, *J. Alloys Compd.*, 2013, **558**, 18.
- 49 R. Rablbauer, R. Fisscher and G. Frommeyer, *Z. Metallkd.*, 2004, **95**, 525.
- 50 Z. Shang, J. Shen, J. F. Zhang, L. Wang, L. S. Wang and H. Z. Fu, *Mater. Sci. Eng., A*, 2014, **611**, 306.
- 51 R. Rablbauer, G. Frommeyer and F. Stein, *Mater. Sci. Eng., A*, 2003, **343**, 301.
- 52 K. A. Jackson and J. D. Hunt, *Trans. Metall. Soc. AIME*, 1966, **236**, 1129.